A Case of Downstream Baroclinic Development over Western North America

I. ORLANSKI AND J. SHELDON

Geophysical Fluid Dynamics Laboratory/NOAA, Princeton University, Princeton, New Jersey

(Manuscript received 1 March 1993, in final form 19 May 1993)

ABSTRACT

Numerical simulations have been made of the initiation of a strong ridge–trough system over western North America and the eastern Pacific (the terminus of the Pacific storm track), with the objective of determining the extent to which downstream development contributed to its growth, and the possible influence of topography on the energetics of the storm. While a control simulation demonstrated considerable skill in reproducing the storm, a "simplified" simulation in which topography, surface heat fluxes, and latent heating were removed not only reproduced the primary features of the ridge–trough system—permitting a clearer interpretation of the factors contributing to its growth—but actually generated a stronger system, suggesting that these effects as a whole inhibited storm development. Application of an energy budget that distinguishes between energy generation via baroclinic processes and generation via the convergence of geopotential fluxes revealed that early growth of the system was dominated by flux convergence. These findings are in agreement with the results of previous studies that have shown that eddies near the downstream end of a storm track grow, at least initially, primarily through the convergence of downstream energy fluxes. Baroclinic conversion, mostly in the form of cold advection, became the primary energy source only after the development was well under way. This sequence of initial energy growth via flux convergence followed by additional contributions by lower-level baroclinic conversion comprise a process designated "downstream baroclinic development" (DBD). A similar analysis of the control simulation showed that the energy budget was essentially the same, with the exception of baroclinic conversion, which was more significant early in the eddy's development due to orographic lifting of warm westerly flow. The decay of the storm in both simulations was mainly the result of flux divergence after the storm reached maturity, although this process was somewhat delayed in the control case because of larger fluxes resulting from the dispersion of additional kinetic energy generated by latent heat release upstream from the system. It is believed that the techniques employed here could represent a valuable new tool in the study of the development of such baroclinic systems and the diagnosis of model deficiencies.

1. Introduction

Recent studies (Orlanski and Katzfey 1991; Orlanski and Chang 1993; Chang and Orlanski 1993) have demonstrated that downstream development could play an important role in the life cycle of baroclinic eddies. Based on the analysis of numerical simulations of storm evolution (Orlanski and Katzfey 1991) and theoretical studies of idealized flows (Simmons and Hoskins 1979; Orlanski and Chang 1993), there has emerged a clearer picture of the role of downstream energy fluxes and local baroclinicity in the growth and decay of baroclinic eddies. Results from single normal-mode studies have led to the belief that mature baroclinic systems decay by frictional dissipation and barotropic conversion to the mean flow. However, it has been found in the "sequential evolution"[1] of baroclinic eddies (Orlanski and Katzfey 1991; Orlanski and Chang 1993) that the principal loss of kinetic energy of individual eddies is actually due to energy dispersion in which kinetic energy is usually collected into a new system downstream. As shown in Orlanski and Chang (1993), a single normal mode will also have flux convergence and divergence but due to its symmetry the net effect is zero. However, sequential evolution requires that many unstable modes be described (Chang and Orlanski 1993). The fluxes in a single eddy are no longer symmetric, so that at each instant, the convergent and divergent regions are not offsetting and the sign of the net flux divergence varies throughout the life cycle of the system. Initial growth of the eddy is accompanied by net convergence. When the eddy matures, the net flux becomes divergent. The behavior of a newly generated eddy depends on both the amount of energy received via these fluxes and the ability to convert surface baroclinicity (due to horizontal temperature gradients) into kinetic energy. Under conditions of *moderate to strong surface baroclinicity* and *very weak downstream fluxes* into the system, the instability grows as a linear baroclinic wave with larger amplitude in the lower layers of the atmosphere in the

[1] "Sequential evolution" refers to the development of localized eddies or groups of eddies that evolve in a limited region of the globe, followed by similar growth in a downstream region, in contrast to single normal modes that simultaneously develop everywhere.

Corresponding author address: Dr. Isidoro Orlanski, NOAA/GFDL, Forrestal Campus, Princeton University, Princeton, NJ 08542.

initial stage of evolution, conforming to our classical notion of baroclinic development. In the case of *large downstream fluxes,* the system initially develops as an upper-level disturbance that quickly organizes the circulation in the lower levels, tapping the surface baroclinicity and leading to further enhancement. Intense cases of this type are typically recognized as so-called class-B cyclogenesis (Petterssen and Smebye 1971). On the other hand, in regions of *very weak baroclinicity,* the system develops primarily as an upper-level disturbance due to downstream fluxes from an upstream eddy. This disturbance has a rather weak signal near the surface, and it is only as the system reaches maturity that the circulation induced near the ground can stimulate baroclinic conversion. In all of these cases, the kinetic energy of the eddy is subsequently lost via fluxes farther downstream, which can then initiate the development of yet another new system. Thus, the role of both downstream energy fluxes and baroclinic conversion can be quite important, both in enhancing the growth of the local eddy and as a source of energy that can be transferred to a new system via geopotential fluxes. For this reason, we define this process as "downstream baroclinic development" (DBD), which refers to the process of *dispersion and spreading of energy in a growing unstable system* and is more characteristic of *high*-frequency baroclinic waves (Orlanski and Chang 1991). This is in contrast to the case where downstream development is associated with the *dispersion of energy by a packet of neutral barotropic* waves more characteristic of *low*-frequency variability (Namias and Clapp 1944; Cressman 1948; Hovmöller 1949; Simmons et al. 1983).

In addition to its importance in the life cycle of individual eddies, downstream baroclinic development has also been shown, using an idealized model (Chang and Orlanski 1993), to play an important role in the maintenance of storm tracks, with downstream radiation of energy through ageostrophic fluxes constituting a primary energy source for the development and maintenance of eddy activity far downstream from the primary baroclinic region. More recently, Chang (1993) applied regression analysis to seven winter seasons using European Centre for Medium-Range Weather Forecasts (ECMWF) data and found that in the Pacific storm track east of the date line, downstream development played a major role in eddy generation. His results are particularly important because other studies using filtered data (Lim and Wallace 1991; Blackmon et al. 1984a,b) failed to show that downstream development could be so important in the generation and decay of high-frequency waves.

Downstream baroclinic development may be involved in a number of observed disturbances that may not be anticipated based solely on an examination of local available baroclinicity. An example of such disturbances that has received considerable attention is the phenomenon of cold outbreaks associated with the eastern Asian monsoon (reviewed by Boyle and Chen 1987). It was suggested by Joung and Hitchman (1982), based on an analysis of composited cases, that such outbreaks correlate with packets of eastward-moving waves originating over North America. They showed that downstream development was responsible for the packet evolution. However, they were unable to determine whether it was baroclinically unstable waves or neutrally propagating barotropic waves that were responsible for the downstream development, since local sources such as surface baroclinicity are very weak in the winter season over the eastern Asian continent. Similar occurrences over the North American continent have not been as extensively studied (Hsu and Wallace 1985) but are of particular interest from the standpoint of downstream development by virtue of being at the downstream end of the Pacific storm track, in the region where Chang's (1993) recent findings indicate that downstream development plays a major role in eddy development. It has been observed that, on some occasions, an intense ridge–trough system develops over the eastern Pacific Ocean and the west coast of North America, drawing frigid air southward over the coastal regions. An extreme example of such an event took place in December 1990 and was chosen to be the subject of the current study because of its robustness, especially given the relatively modest precipitation (and hence modest latent heating). It was also a rather severe weather event, setting many all-time record lows and bringing the first freeze to California since the 1936/37 growing season, and therefore deserving of special attention. The system also appeared to be strongly affected by topography, an issue of considerable interest regarding the manner in which the Pacific storm track terminates at the North American continent. The focus of this paper will be on determining the processes involved in the initial development of this intense ridge–trough system.

The evolution and characteristics of the December 1990 event are described in section 2, along with the numerical model used for the simulation of the event. Section 3 discusses the results of two simulations, a control case and a "simplified" case in which a number of forcing influences (e.g., topography, surface heat flux, etc.) are eliminated. Section 4 presents a derivation of the eddy kinetic energy budget and the role of geopotential fluxes, and then applies this budget to the two simulations. A summary is provided in section 5.

2. Analysis

a. Description of the December 1990 event

Frigid air overran much of the western half of the United States for the latter half of December 1990. *The Weekly Climate Bulletin* (29 December 1990) reported that hundreds of weather stations had set daily minimum temperature extremes, with several having established record December low temperatures aver-

aging 5°–13°C below normal. California was especially hard hit, with temperatures plunging well below freezing, reaching minimum temperatures as low as −10°C. We shall first examine the characteristics of the flow leading up to such an extreme event.

The evolution of the Ertel potential vorticity field (hereafter denoted "PV") on the 310-K isentropic surface (approximately 400–500 mb at 50°N) over the Pacific and North America during the period 0000 UTC 16 December to 0000 UTC 23 December is shown in Fig. 1, derived from the National Meteorological Center (NMC) analyses. The pattern was characterized by relatively zonal flow over the northern half of the domain early in the period. Over the southern half of the domain, there were moderate ridges at 170° and 220°E. Troughs were present at 185° and 245°E, denoted "B" and "C," respectively. In the ensuing 48 h, a trough developed in the gulf of Alaska ("A") accompanied by strong ridging over the central and eastern Pacific. By 0000 UTC 19 December, trough A moved southeast along the western North American coast, and by 0000 UTC 20 December, a very intense ridge in the eastern Pacific extended to the northeast as trough A achieved its maximum intensity, reaching as far south as southern California and Arizona (35°N). After this time, the northern portion of the ridge translated northeast and trough A became cutoff over the southwestern United States; then it eventually moved northeast across the Great Lakes. The ridge persisted through 23 December, retaining significant amplitude over the eastern Pacific.

b. *Model description*

This event has been simulated using the Geophysical Fluid Dynamics Laboratory (GFDL) limited-area model (LAHM) with the GFDL physics package. [See Orlanski and Katzfey (1987) for a more complete description of the model.] The LAHM is a primitive equation sigma coordinate model employing a latitude–longitude E grid (Mesinger 1977, 1981). In this case, 18 vertical levels were used. The model physics is similar to the E2 physics of the GFDL global model (Miyakoda and Sirutis 1977) and includes radiation, Arakawa–Schubert convective parameterization, and soil and sea-ice surface parameterization. Vertical turbulent transfer is handled via Mellor–Yamada level 2.0 turbulent closure. The lateral boundary conditions use time tendencies of the dependent variables interpolated in time and space from 2.5° × 2.5° NMC analyses. Model initial conditions are provided by the NMC analysis, with hydrostatic adjustment of the temperature field. (Note that NMC analyses include extrapolations to levels below ground.) Sea surface temperatures were derived from the December monthly mean climatological values. The only modification made to the baseline LAHM was an increase of the drag coefficients C_D in high terrain. The coefficients for momentum, heat, and moisture were increased by a factor of 6 for ground heights above 500 m, resulting in (momentum) C_D values on the order of 30×10^{-3} to 50×10^{-3} over the Rockies. This modification resulted in a more realistic simulation of the flow over the Rocky Mountains and was but one of many that were examined as part of a sensitivity analysis, the results of which will be published elsewhere.

3. Simulation results

a. *Control simulation*

A 72-h "control" simulation using the baseline LAHM (with the modified C_D values as discussed above) was performed using as initial conditions the NMC analysis for 0000 UTC 17 December, and a domain of 20°–80°N, 160°–276°E. This time was chosen because trough A (Fig. 1) was clearly identifiable but its development was only just beginning. In addition, since there was no hint of a preexisting trough ahead of trough A at that time (trough C moved away from the region of interest and did not interact with trough A), the strong development over the subsequent 72 h can be entirely attributed to trough A. Since our main interest is the onset of the large ridge–trough pattern, our discussion will focus primarily on the first 48 h.

A comparison between the simulation and the analysis is shown in Fig. 2, which depicts the height of the 500- and 850-mb surfaces at 0000 UTC 19 December (48 h). The left panels show the analyzed 500- and 850-mb height fields at 0000 UTC 19 December, and the right panels show the corresponding fields for the simulation. The large ridge at 210°E is quite evident, and trough A has intensified considerably by this time. The major features of the storm development were captured quite well by the model, including the building of the strong ridge in the eastern Pacific and the development of a compact low-level cyclone over Puget Sound. Some deficiencies can be found in the simulated ridge—which, at 500 mb, is somewhat weaker over the eastern Pacific than indicated in the analysis—and the 500-mb short-wave trough over Puget Sound—which is not as pronounced. At low levels, the model tended to overdeepen the storm in the lee of the mountains and did not deepen it enough on the windward side. It should be noted that most operational models also tend to have relatively poor forecasting skill in this particular region (Smith and Mullen 1993). Although the question of whether poor data and/or topography are the cause of the reduced forecast skill in this region is a valid question worth investigating, the focus of this paper is on the processes contributing to the development of the large trough–ridge system, and issues regarding model forecast skill and its sensitivity to model physics will be published elsewhere. Nevertheless, in general, the model did a reasonable job capturing the system, thereby providing the confidence needed to

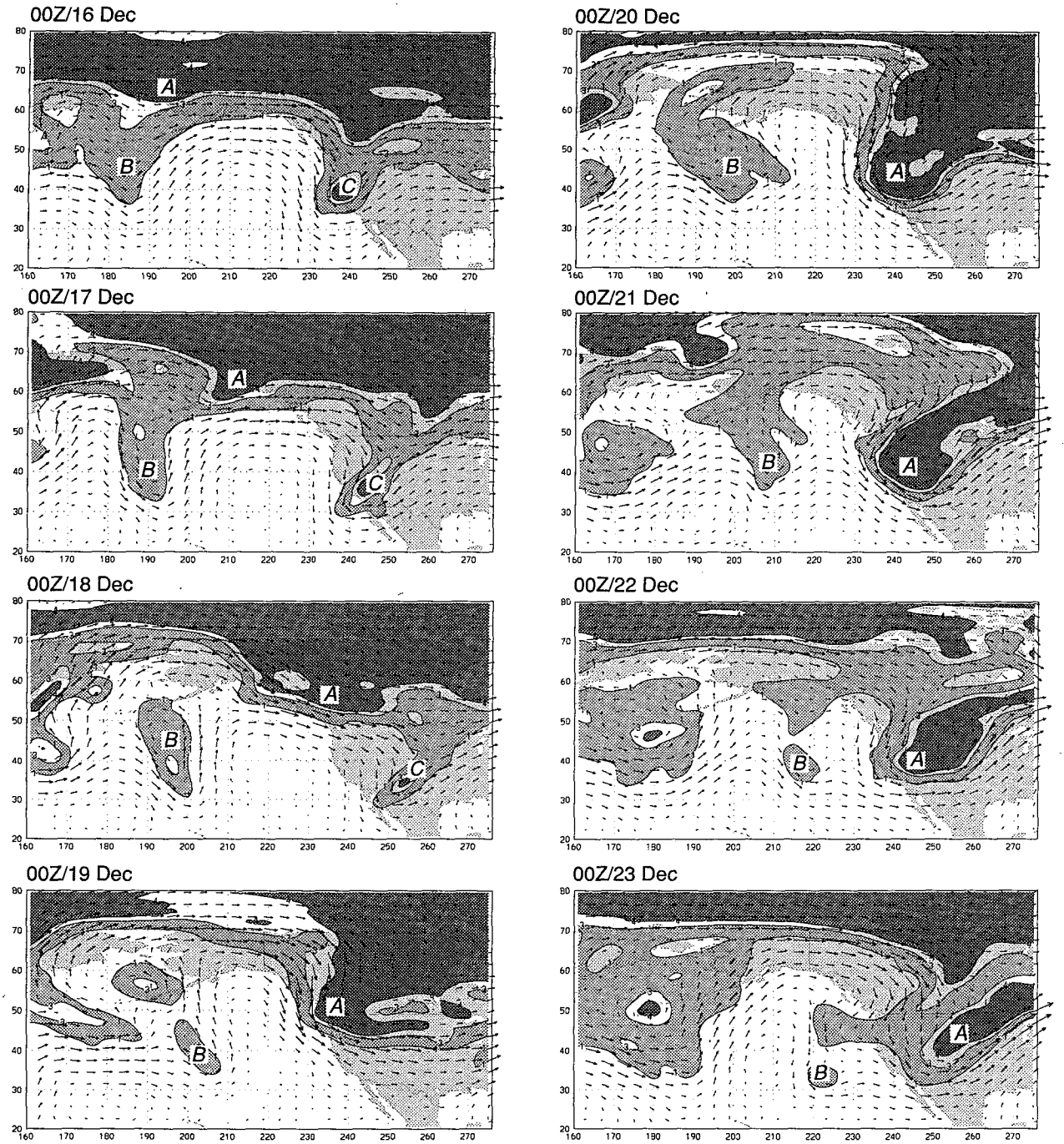

FIG. 1. Time sequence of isentropic potential vorticity and wind on the 310-K potential temperature surface, from 0000 UTC 16 December 1990 to 0000 UTC 23 December 1990. Light shading indicates PV range of 1–3 PV units (10^{-6} m^2 K kg^{-1} s^{-1}); dark shading indicates PV greater than 4 PV units. Letters A, B, and C indicate troughs discussed in text.

proceed with an investigation of the factors influencing its evolution and an assessment of its energetics.

Given the location and orientation of the flow in this case, it would appear that land–sea contrast and orography is likely to have played an important role in the evolution of the trough. In fact, in a statistical analysis of cold outbreaks accompanying large trough patterns over northern North America, Hsu and Wallace (1985) found a strong orographic blocking effect. A large number of exploratory simulations were conducted in order to assess the factors influencing the evolution of this system. Effects that were investigated

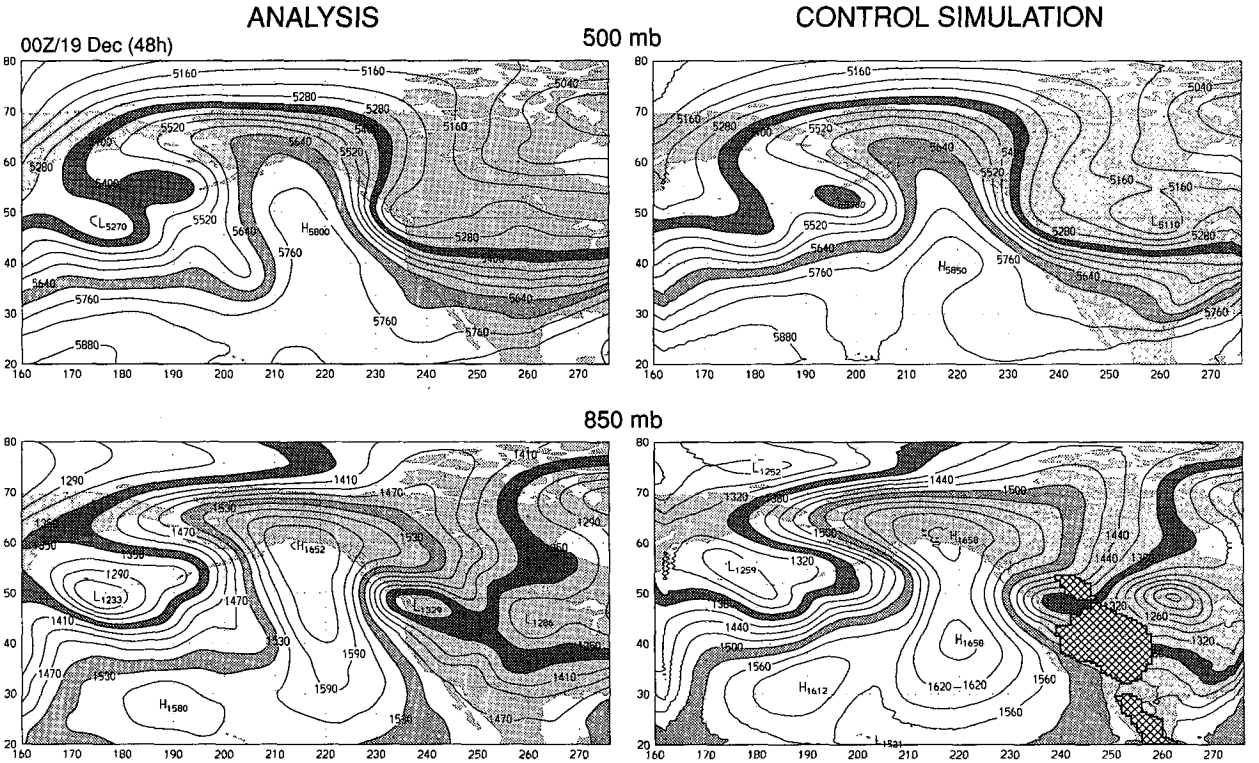

FIG. 2. The 500-mb (top panels) and 850-mb (bottom panels) heights at 0000 UTC 19 December. Left panels are NMC analyses; right panels are for the control simulation (at 48 h). Contour intervals are 60 and 30 m for the 500- and 850-mb maps, respectively. For the 500-mb field, light and dark shading corresponds to heights between 5640 and 5700 m and 5340 and 5400 m, respectively. For the 850-mb field, light and dark shading corresponds to heights between 1500 and 1530 m and 1350 and 1380 m, respectively. Hatched area at 850 mb for the simulation indicates surface is below ground.

included topography, land versus ocean surface, drag coefficient variations, presence or absence of latent heating, surface heat flux variations, and surface momentum flux variations. The parametric space examined revealed some quantitative differences but remarkably minor qualitative differences. However, the most striking result was that even the most simplified simulation (no land, no surface heat flux, no latent heating; described in the following section) was able to capture the essence of the evolution of this large PV feature.

Sensitivity experiments such as this, in which drastic simplification or elimination of processes are made, are common practice in studies where numerical models are used to determine the dynamical characteristics of an event. The reasons for analyzing a simplified simulation, assuming it has captured the qualitative features related to the building of the ridge–trough system, are twofold. First, the lack of boundary forcing and diabatic effects make for a system that is easier to describe and analyze. Second, the energetics concepts to be applied in this study are rather new and are more easily introduced for a simpler system. However, we will return to an analysis of the control simulation in section 4 to assess the influence of topography, heat fluxes, and latent heating.

b. *"Simplified" simulation*

In this simulation, all land surface, latent heating, and sensible and latent heat fluxes were eliminated, and the drag coefficient was held constant at 10^{-3}. The initial time was the same as the control, with initial conditions and boundary conditions derived from NMC analyses. It should be pointed out that while the initial conditions, per se, do not include any topographic boundary or surface forcing, the initial conditions will retain some "memory" of the stationary response forced by the true topography and land–sea contrast. However, as discussed previously, inspection of the PV distribution for the initial state (0000 UTC 17 December, see Fig. 1) shows that the only trough over the western United States observed at the initial time (trough C) decays as it is advected eastward and does not interact directly with the system of interest. Also, there is little evidence of the large-scale ridge–trough pattern that will evolve over the entire Pacific over the next few days.

The results at the end of 48 h of simulation are shown in Fig. 3, again depicting the 500- and 850-mb height fields. The fields in Fig. 3 can be directly compared with those of the control solution or the analysis at the same time (see Fig. 2). A comparison with the analysis

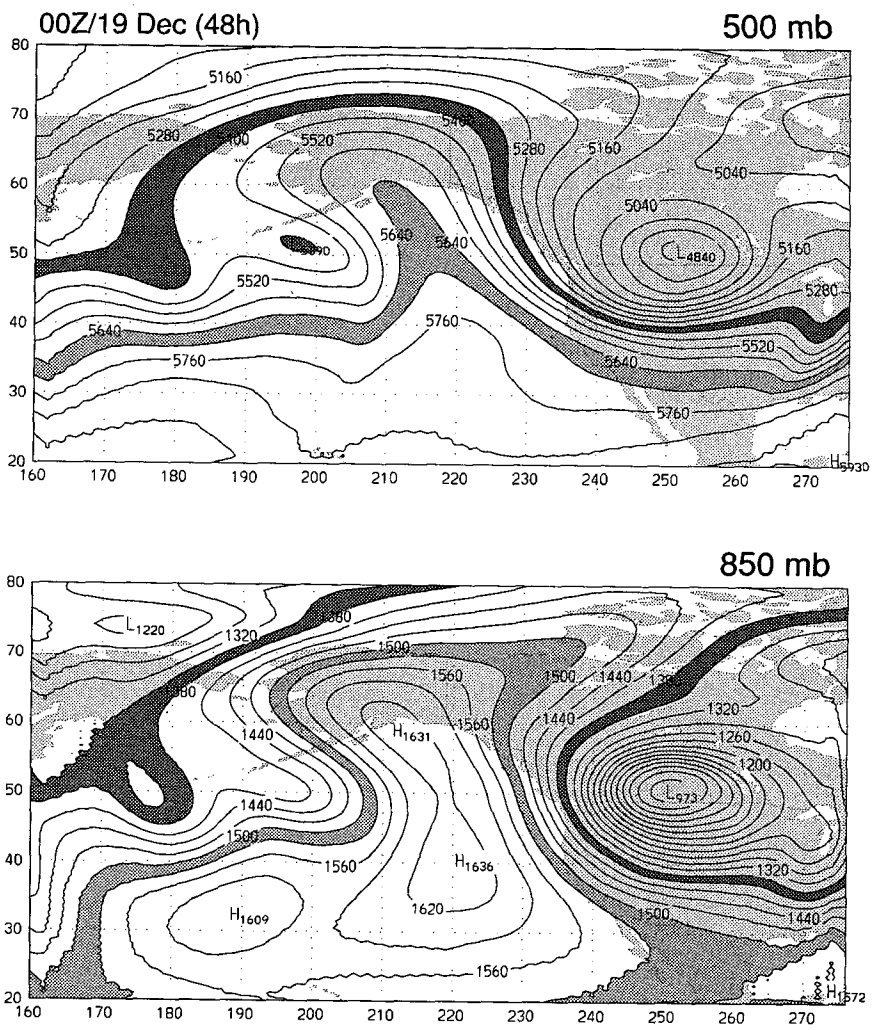

FIG. 3. The 500-mb (top) and 850-mb (bottom) heights at 0000 UTC 19 December for the simplified simulation. Contour interval and shading as in Fig. 2.

and control simulation reveals that the *removal* of such factors as land–sea temperature contrast, topographic forcing, variable surface friction, and latent heating (many of which are considered to be positive influences for storm development) actually led to the development of a *stronger* system. Following the surface low as it moved onshore from the eastern Pacific, the evolution of the minimum sea level pressure for the analysis and the two simulations during the first 48 h are shown in Fig. 4. The simulations resemble each other more than either one resembles the analysis for the first 15 h, with both simulations deepening slowly, as opposed to the analysis, which showed a slight filling. After that time, however, the control simulation showed better agreement with the analysis, with central pressures equal at 24 h and deepening slowly thereafter, in contrast to the analysis, which filled slightly. The "simplified" simulation deepened rapidly after 15 h, reaching a central pressure approximately 30 mb lower than the analysis and 23 mb lower than the control simulation. Note, however, that since the surface low pressure center lies over mountainous terrain between 18 and 30 h, sea level pressure comparisons should be viewed only as a nominal indicator of storm strength. As noted previously, sizable model errors in the sea level pressure are common in this region, and the errors in the present (control) simulation are of the same order of magnitude as those typical of the NMC Nested Grid Model (NGM), which displays a standard deviation of pressure error of nearly 7 mb in this region (Smith and Mullen 1993).

The volume-integrated kinetic energy provides a more comprehensive measure of the system's development and is shown in the lower panel of Fig. 4. The volume used, which is arbitrary, follows the K_e maximum and is bounded in the vertical by the ground surface (pressure = p^*) and the 50-mb model top, and in the horizontal by the 600 m^2 s^{-2} contour of the ver-

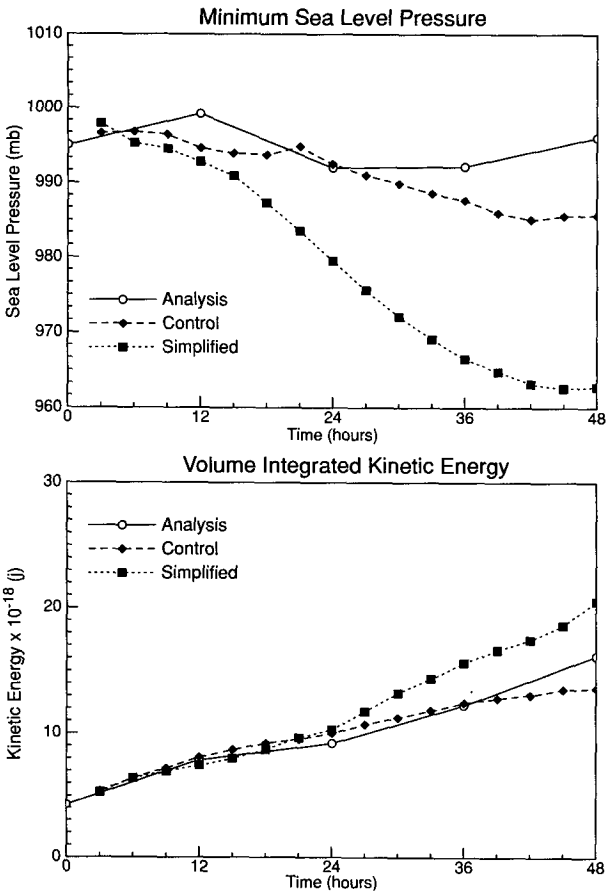

FIG. 4. Evolution of sea level pressure (mb, top) and volume-integrated kinetic energy (10^{18} J, bottom) for the 48-h period from 0000 UTC 17 December to 0000 UTC 19 December. Solid, dashed, and dotted lines are for the analysis, control simulation, and simplified simulation, respectively. Integration volume for kinetic energy is bounded in the vertical by the model top (pressure = 50 mb) and the ground surface, and in the horizontal by the 600 $m^2 s^{-2}$ contour of vertically averaged kinetic energy.

tically averaged kinetic energy (50 mb to p^*). The integrated kinetic energy for both simulations tracks that of the analysis very closely for the first 24 h. Thereafter, the control simulation grows at a slightly lower rate than the analysis, while the simplified simulation grows faster than the analysis. However, the differences are far less pronounced than noted with respect to the sea level pressure. It appears that while topography disrupts the baroclinic development of the surface system, the kinetic energy, dominated by the upper levels, is basically the same. This result is consistent with other studies (Orlanski and Gross 1993, and others) of the detrimental effects of orography on the primary baroclinic development. In any case, eliminating the influence of topography (as well as surface drag variations, surface heat fluxes, and latent heating) facilitates a much clearer interpretation of the processes involved in the basic evolution of this weather pattern.

Finally, to remark further on the similarity of the simulations at upper levels, a comparison of the 310-K potential vorticity and velocity patterns for the two simulations at 48 h is shown in Fig. 5. The patterns are obviously quite similar, although the greater strength of the "simplified" system is evident in the area of the Rocky Mountains. That portion of the ridge over Alaska and northwest Canada is basically the same in both simulations. There are, however, some noticeable differences in the velocity and the PV distribution over the western Pacific. These differences were likely due to the cumulative effect of eliminating latent heat release (which was a significant source of energy for the developing system in the western Pacific) and heat fluxes from the surface to the air as the system passed over the southwestern North Pacific.

Local energy budget analyses have proven to be a useful diagnostic tool for distinguishing the role of different processes in the development of baroclinic systems (Orlanski and Katzfey 1991; Orlanski and Chang 1992; Chang and Orlanski 1993). The energy budget for this simulation has been performed and the results are discussed in the next section.

4. Energetics

In this section, an eddy energy budget is computed by defining "eddies" as deviations from a "mean" flow. This mean flow could be either the time or the zonal mean. In general, the time mean flow is preferable because it would represent better the local effects present in a particular region (Orlanski and Katzfey 1991). However, since we are interested in calculating the energy budget of the simplified solution as well as the control, use of a time mean would require the calculation of a solution over a long enough period to derive a compatible time mean. This option is not practicable, and for that reason the zonal mean will be used instead for both cases. The derivations of the energy equations is very similar to that in Orlanski and Katzfey (1991), and the details will not be repeated here.

a. Eddy kinetic energy equation

1) PARTITIONING OF THE KINETIC ENERGY EQUATION

The energy budget is divided into a zonal mean part (for the length of the simulation domain, which is 116° of longitude in the present case) and an eddy part by partitioning the velocity and thermodynamic variables as follows:

$$\mathbf{V} = \mathbf{V}_m + \mathbf{v}$$
$$Q = Q_m + q, \qquad (4.1)$$

where the $\mathbf{V}$ is the horizontal wind; Q is any scalar, including the vertical velocity ω; and the subscript m

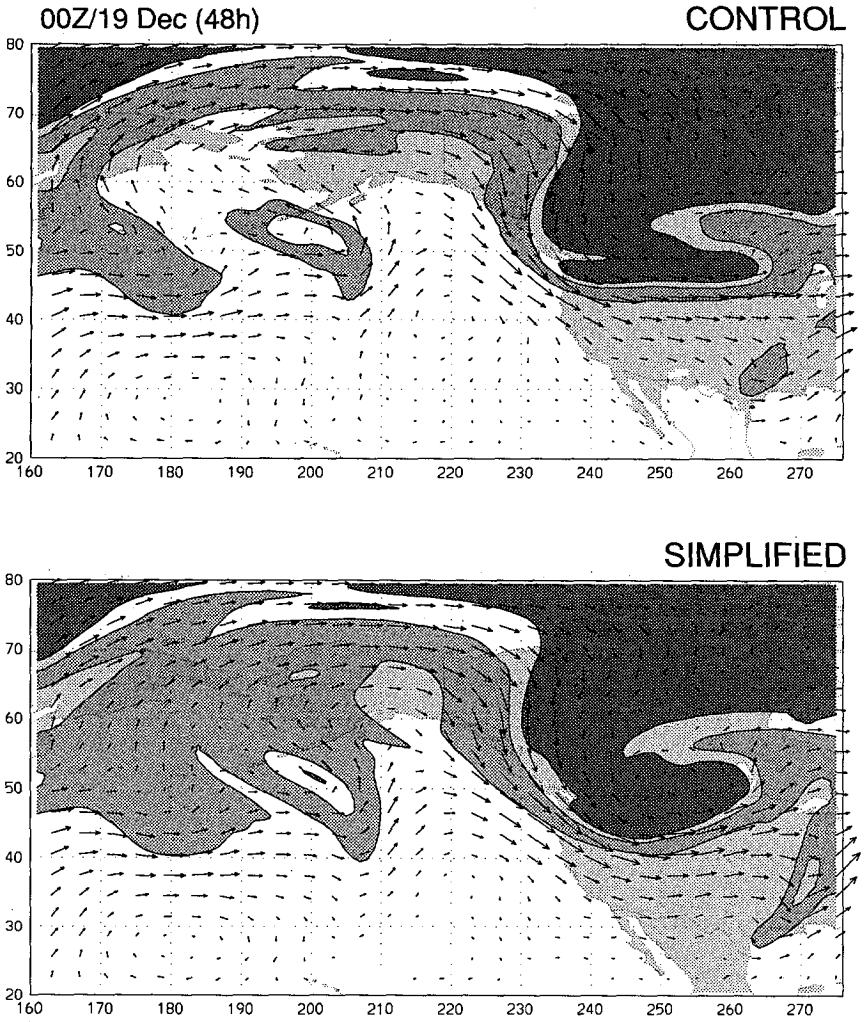

FIG. 5. Potential vorticity and wind on the 310-K potential temperature surface for the control (top) and simplified (bottom) simulations at 0000 UTC 19 December 1990 (48 h). As in Fig. 1, light shading indicates PV range of 1–3 PV units; dark shading indicates PV greater than 4 PV units.

indicates the zonal mean. [Note that $\mathbf{V}_m$ is defined here as $(U_m, 0, 0)$.]

The eddy kinetic energy equation in pressure coordinates is given by

$$\frac{\partial K_e}{\partial t} = -(\mathbf{v}\cdot\nabla\phi) - [\nabla\cdot(\mathbf{V}K_e)] - \frac{\partial(\omega K_e)}{\partial p} + \text{residue}, \tag{4.2}$$

where $K_e = (1/2)|\mathbf{v}|^2$. The term on the left is the tendency of eddy kinetic energy, and the terms on the right are the advection of eddy geopotential heights by the eddy velocity, and the horizontal and vertical divergence of the eddy kinetic energy fluxes. Two other terms, $\mathbf{v}\cdot(\mathbf{v}\cdot\nabla\mathbf{v})_m$ and $\mathbf{v}\cdot(\mathbf{v}\cdot\nabla\mathbf{V}_m)$, as well as dissipation, are all included in the "residue" term.

2) AGEOSTROPHIC GEOPOTENTIAL FLUXES

Orlanski and Katzfey (1991) showed that the first term on the rhs of (4.2) can be written as

$$-\mathbf{v}\cdot\nabla\phi = -\nabla\cdot(\mathbf{v}_{a0}\phi) - \omega\alpha - \frac{\partial(\omega\phi)}{\partial p}. \tag{4.3}$$

Since the eddy geostrophic wind $\mathbf{v}_{g0}$ (defined using a constant f_0) is nondivergent, the flux defined by the ageostrophic velocity $\mathbf{v}_{a0}$ is

$$\mathbf{v}_{a0}\phi = \mathbf{v}\phi - \frac{\mathbf{k}}{f_0}\times\frac{\nabla\phi^2}{2}. \tag{4.4}$$

Note that the last term in (4.4) is the geopotential field multiplied by the geostrophic velocity (geostrophic geopotential flux), which is obviously nondivergent. It

is clear, then, that the geopotential fluxes defined using the ageostrophic velocity $\mathbf{v}_{a0}$ will retain the entire divergent component of the total flux $\mathbf{v}\phi$.

The first term on the rhs of (4.3) is the divergence of the ageostrophic geopotential fluxes and represents the dispersion of energy. The second term, $\omega\alpha$, represents (in an averaged sense) the conversion of available eddy potential to kinetic energy. The third term is the vertical flux divergence that redistributes energy vertically via work done by pressure forces. The vertical integral of this term over the entire atmosphere is usually very small.

When the latitudinal extent of the domain becomes large (in this case, 60°), the "ageostrophic" velocity $\mathbf{v}_{a0}$ will contain a large portion of the geostrophically balanced flow for latitudes considerably different than that selected for defining the constant Coriolis parameter f_0 [see (4.4)]. Of course, only the convergence/divergence of those fluxes has any importance for the energy balance, but the flux vector itself becomes less useful as an indicator of the direction of energy flow. Orlanski and Chang (1993) showed that, for constant $f = f_0$, the ageostrophic flux vector in an average sense (i.e., averaged over an eddy) is approximately parallel to the trajectory of the energy packet or (in the small-amplitude limit) to the relative group velocity. However, when f is truly variable, the use of a constant f_0 in (4.4) will yield fluxes that contain a large nondivergent component at latitudes away from that corresponding to f_0, obscuring the direction of the net energy flow. A slight modification in the definition of the nondivergent component of the geopotential fluxes will extend (4.4) to the case of a variable Coriolis parameter:

$$(\mathbf{v}\phi)_a = \mathbf{v}\phi - \mathbf{k} \times \nabla \frac{\phi^2}{2f(y)}. \qquad (4.5)$$

It is easy to see that the removed flux is still nondivergent and reduces to the expression defined in (4.4) when f is constant. A expression similar to that in (4.5) was derived for small-amplitude Rossby waves in a shallow-water model (Longuet-Higgins 1964; Pedlosky 1987), and it was shown that those fluxes are parallel to the relative group velocity. As a side note, the simplicity with which the large nondivergent part of $\mathbf{v}\phi$ can be removed contrasts sharply with the analogous procedure for PV. It may be that PV anomalies are such good indicators of weather patterns that the fluxes of PV could be an important diagnostic tool for determining the source and sink regions of PV. However, PV fluxes represented in a manner analogous to the geopotential fluxes presented here contain a strong geostrophic rotational component that, unfortunately, is not easily removed. Although this component will have no effect on the divergence of the fluxes, it will make it more difficult to use the flux field as an indicator of the direction of energy flow. Hence, we will use geopotential fluxes as our diagnostic tool, and we will make extensive use of the flux vectors defined by (4.5) in the following discussions.

b. *Simplified simulation*

1) THE EDDY KINETIC ENERGY BUDGET

Selected contours of vertically averaged eddy kinetic energy K_e and the total eddy energy fluxes $(\mathbf{v}\phi)_a + \mathbf{V}K_e$ for 12 and 36 h are shown in Fig. 6, which clearly illustrates the connection between the fluxes and the eddy energy centers. The positions of troughs A, B, and C noted in Fig. 1 are also shown. The main area of interest is intensification of the energy center on the eastern side of trough A. The small maximum in eddy kinetic energy present at 1200 UTC 17 December (12 h) grows explosively in the subsequent 24 h. If the fluxes are interpreted as an energy flow, one sees that the incipient K_e center is being fed by a larger center to its southwest (around 200°E), which decays over the following 24 h but nevertheless maintains these fluxes to the growing system. To better understand the different sources and sinks of eddy kinetic energy that are associated with the growing energy center, we will calculate the individual terms of (4.2) and, for clarity, focus our attention on the area within the heavy dashed rectangle in Fig. 6.

Figure 7 shows the vertically averaged (50 mb to p^*) distributions of (a) eddy kinetic energy tendency, (b) convergence of the advected fluxes $-\nabla \cdot (\mathbf{V}K_e)$, and (c) $-\mathbf{v} \cdot \nabla\phi$ at 12 h. The vertically averaged $K_e = 300$ $m^2\ s^{-2}$ contour (arbitrary value) is also shown. The heavy contour encloses the energy center for which volume integrals are to be presented later. Note first that the eddy kinetic energy tendencies within the area limited by the reference contour are predominantly positive, consistent with the fact that system is in the growing stage. Second, both $-\nabla \cdot (\mathbf{V}K_e)$ and $-\mathbf{v} \cdot \nabla\phi$ contribute significantly to the net tendency. The pattern of $-\nabla \cdot (\mathbf{V}K_e)$ shows strong convergence at the downstream end of the center and strong divergence upstream. The $\mathbf{V}K_e$ flux vector field indicates that the depletion of energy in the rear is balanced by accumulation in the front of the eddy energy center. Obviously, this effect results mainly in the translation of the system. The field of $-\mathbf{v} \cdot \nabla\phi$, however, possesses a strong asymmetry, displaying an area of strong generation in the entrance region of the energy center [commonly referred to as a "jet streak," after Uccellini (1985)] with a smaller, less intense region of dissipation at the exit region. The large positive area of $-\mathbf{v} \cdot \nabla\phi$ correlates well with the convergence of the ageostrophic fluxes, and a negative area to the west correlates well with flux divergence there.

To summarize, Fig. 7 shows that, for the energy center defined by the reference K_e contour, there is a net increase of K_e via $-\mathbf{v} \cdot \nabla\phi$ and a redistribution of energy from the rear to the front of the center by the $\mathbf{V}K_e$

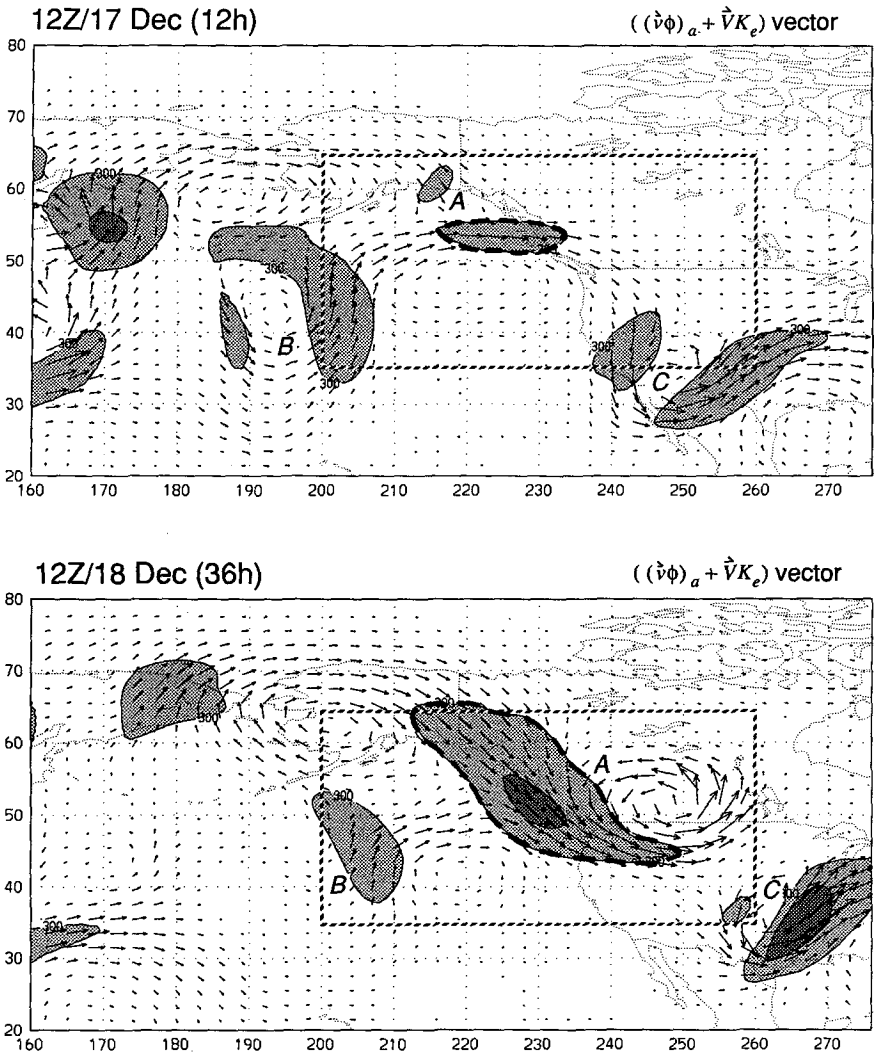

FIG. 6. Vertically averaged eddy kinetic energy and energy fluxes for the simplified simulation at 12 and 36 h. Shaded areas are 300–600 $m^2 s^{-2}$ (light) and greater than 600 $m^2 s^{-2}$ (dark). Energy flux vectors are represented as $[(\mathbf{v}\phi)_a + \mathbf{V}K_e]$. Letters A, B, and C correspond to the troughs depicted in Fig. 1. Dashed box indicates subregion to be shown in subsequent figures. The heavier dashed contour indicates the bounds of the specific volume of integration to be addressed later.

fluxes, resulting in a net positive tendency. Note also that the $\mathbf{V}K_e$ field is large *within* the center, whereas $(\mathbf{v}\phi)_a$ are large *between* energy centers, a phenomenon that will become increasingly apparent. It is clear (at least from Fig. 7) that the K_e fluxes result primarily in the *translation* of the energy center, while the primary (Lagrangian) source of energy of the *growth* of the energy center is $-\mathbf{v}\cdot\nabla\phi$. The key question at this point is whether the strength of $-\mathbf{v}\cdot\nabla\phi$ in this case was due to geopotential flux convergence, $-\nabla\cdot(\mathbf{v}\phi)$, or baroclinic conversion, $-\omega\alpha$ [as shown in (4.3)].

2) THE BUDGET OF $-\mathbf{v}\cdot\nabla\phi$

Figure 8 addresses the question posed above and shows (bottom panel) that the $\omega\alpha$ contribution is very small at this initial time and that the convergence of $\mathbf{v}\phi$ is virtually the sole contributor to energy generation via $-\mathbf{v}\cdot\nabla\phi$. One can see that the strong convergence of $(\mathbf{v}\phi)_a$ in the new center is, in large part, balanced by divergence in the rather mature system to the southwest. Thus, energy dispersed from the decaying energy center upstream contributes to the initial development of the growing energy center that it is associated with the development of the downstream trough. Note also that, as previously discussed, the vectors $(\mathbf{v}\phi)_a$ clearly indicate the direction of this energy dispersion.

The distribution of K_e tendency, $-\mathbf{v}\cdot\nabla\phi$, and $-\nabla\cdot(\mathbf{V}K_e)$ at 36 h (not shown) indicates that as the integrated K_e approaches its maximum the net local

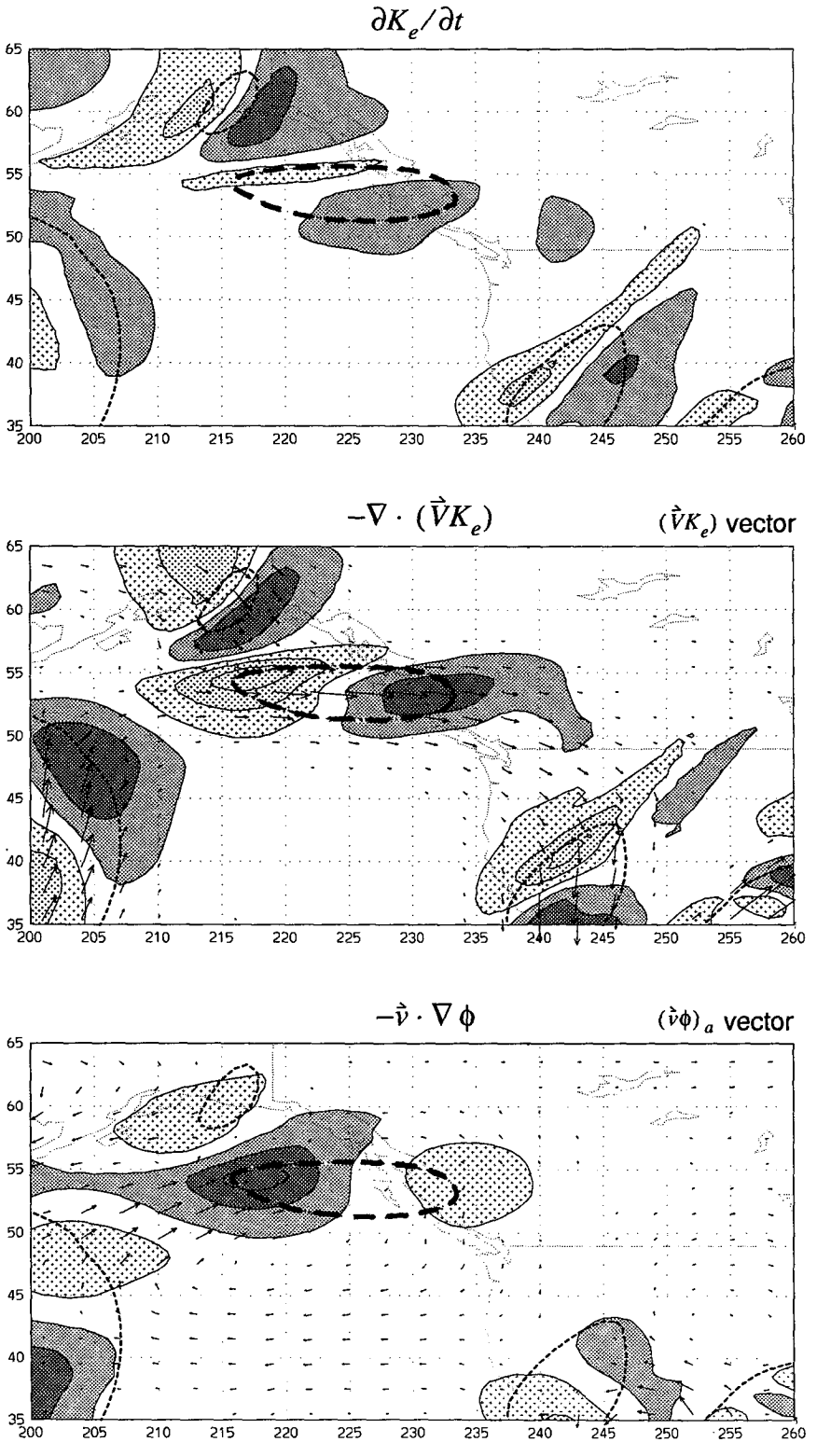

FIG. 7. Vertically averaged energy tendency terms ($m^2 s^{-3}$) for the simplified simulation at 1200 UTC 17 December (12 h). Top panel: $\partial K_e/\partial t$; middle panel: $-\nabla \cdot (\mathbf{V}K_e)$; bottom panel: $-\mathbf{v} \cdot \nabla \phi$. Stippled areas indicate energy loss, light stippling: -0.01125 to -0.00375, dark stippling: less than -0.01125. Shaded areas indicate energy gain, light shading: 0.00375 to 0.01125, dark shading: greater than 0.01125. The dashed lines are the vertically averaged eddy kinetic energy of 300 $m^2 s^{-2}$ contour. The heavier dashed contour indicates the bounds of the specific volume of integration to be addressed later.

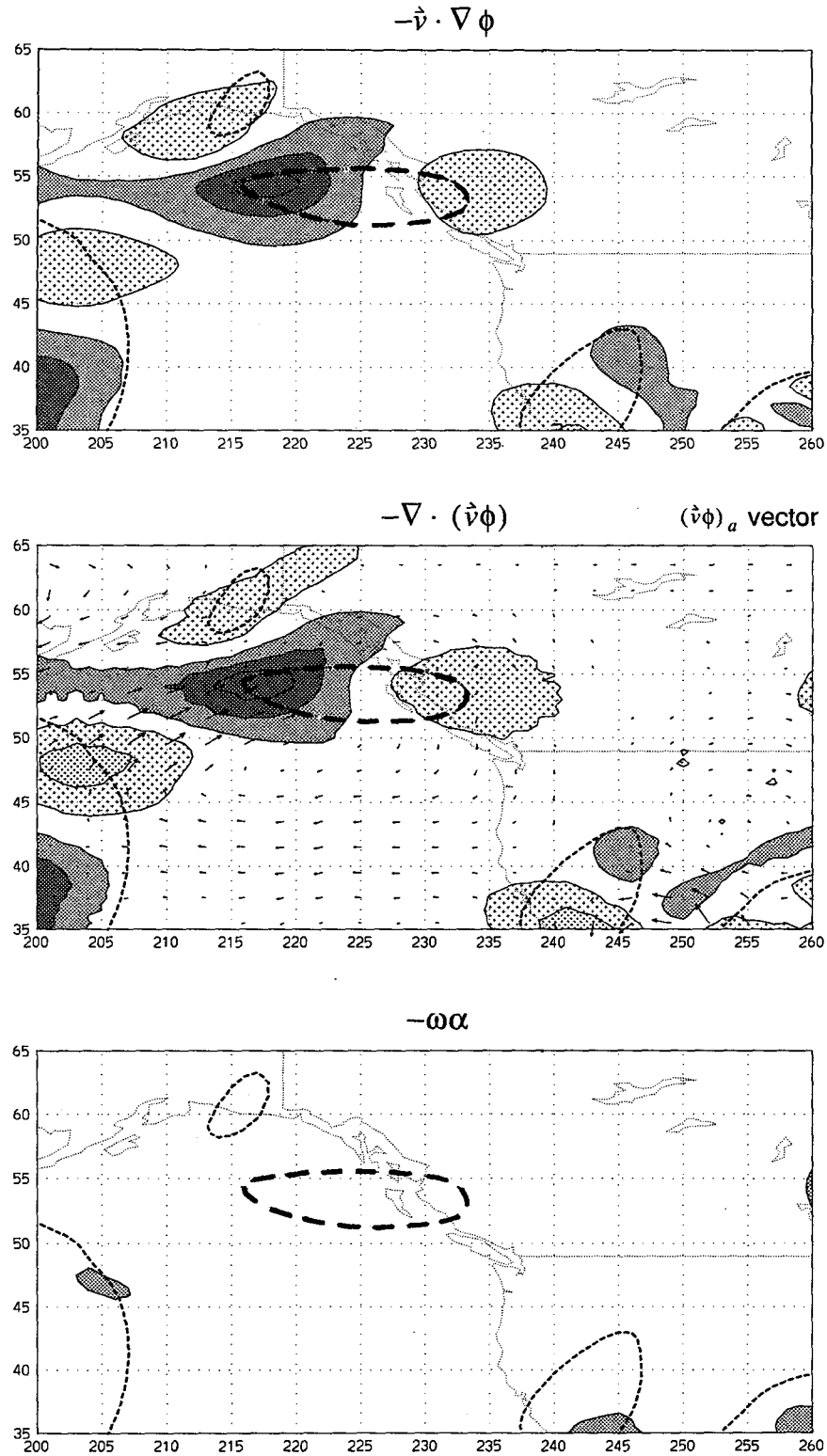

FIG. 8. Vertically averaged components of $-\mathbf{v}\cdot\nabla\phi$ for the simplified simulation at 1200 UTC 17 December (12 h). Top panel: $-\mathbf{v}\cdot\nabla\phi$ (repeated from Fig. 7); middle panel: $-\nabla\cdot(\mathbf{v}\phi)$ and $(\mathbf{v}\phi)_a$ vector field; bottom panel: $-\omega\alpha$. Units, stippling, and shading same as in Fig. 7. The heavier dashed contour indicates the bounds of the specific volume of integration to be addressed later.

tendencies inside the volume are small and that the energy advection at this time displays convergent and divergent regions similar to that at 12 h. The $-\mathbf{v}\cdot\nabla\phi$ term and its components are shown for this time in Fig. 9. The distribution of $-\mathbf{v}\cdot\nabla\phi$ shows large positive and negative areas, but the net contribution remains positive (albeit small). The distribution of $-\nabla\cdot(\mathbf{v}\phi)$ still dominates the overall pattern and, as before, the area of convergence is on the western side of the K_e center, with the divergent fluxes (much stronger now) at the eastern end of the system. Thus, while the K_e center seems to receive energy from fluxes from the upstream center, it also begins to disperse a significant amount of energy downstream. At the same time, baroclinic conversion is intensifying, with $\omega\alpha$ now larger and contributing to maintain positive $-\mathbf{v}\cdot\nabla\phi$. Discussion of the relative contributions of the terms in (4.2) and (4.3) for this 48-h period of evolution of the K_e center follows.

3) EVOLUTION OF THE ENERGETICS

The results displayed in Figs. 6–9 provide a clear view of the local contributions of each term in (4.2) and (4.3) at specific times. However, it is important to evaluate the role of each term throughout the evolution of the system. If K_e were conservative, then we could follow a given volume bounded by a K_e contour and the results would be truly Lagrangian, following particles with constant K_e. Although this is not possible, neither is it necessary, since we can calculate all the necessary terms in (4.2). However, a more difficult problem, from the standpoint of integrating the contributions, is the definition of the volume over which the integrals are evaluated. This definition cannot be altogether arbitrary, since any results could be quite sensitive to the placement and extent of the volume. Integrating over the entire model domain does not make sense, since combining all the evolving centers in the domain would not be very enlightening. A more objective and pragmatic approach was used by Orlanski and Katzfey (1991), in which they followed a volume bounded by a given contour of vertically averaged K_e, which encompasses the K_e center of interest. This definition is quite reasonable, since the volume thus defined will be translated with a speed similar to that of the main cyclone–anticyclone system and, as mentioned earlier, all boundary fluxes can be accounted for. A desirable feature of this definition is that the volume remains unique along the period of integration. Nevertheless, we recognize that a somewhat less arbitrary definition may be more robust, and this topic is, at present, under investigation.

Taking as a volume definition the region bounded in the vertical by the earth and the 50-mb surfaces and in the horizontal by the vertically averaged K_e contour (300 $m^2\ s^{-2}$), integrals were calculated of all of the terms in (4.2) and (4.3). Figure 10 shows the first 48 h of evolution of the volume-integrated K_e (upper panel), the volume integral of the terms defined in (4.2) (middle panel), and the integrated contributions of the terms in (4.3) (lower panel). During this time, K_e grew by more than a factor of 10, reached its maximum amplitude, and started to decay. The normalized contributions of each term in (4.2) (integrals were divided by the volume integral of K_e) are shown as growth rates. The time tendency of K_e is positive and large at the beginning of the period, in agreement with the evolution of K_e in the upper panel. This tendency is composed of $-\mathbf{v}\cdot\nabla\phi$, $-\nabla\cdot(\mathbf{V}K_e)$ and a "residue" that, as explained earlier, contains all other terms in the eddy kinetic energy equation. The main contribution to this residue comes from surface dissipation (recall that a constant $C_D = 10^{-3}$ is used in the simplified solution) and is always negative. Consistent with the previous discussion, it is clear that $-\mathbf{v}\cdot\nabla\phi$ represents the largest source of energy, with its contribution being very large at the initial times, then tapering off, and becoming negative later. Note also that since the chosen volume follows closely the translation of the system, the net contribution of $-\nabla\cdot(\mathbf{V}K_e)$ is relatively small. Also consistent with the previous discussion is the result that the main contributor to $-\mathbf{v}\cdot\nabla\phi$ in the developing stages is $-\nabla\cdot(\mathbf{v}\phi)$ (see lower panel of Fig. 10), which shows net normalized convergence at early stages, then decreases and becomes divergent at the later stages. The baroclinic contribution $\omega\alpha$ is consistently positive, becoming the main source of energy only when the system has matured and starts to decay. However, its magnitude is small and, toward the end of the 48-h period, is not sufficient to increase the K_e of the system, since its contribution is offset by the net divergence of the $\mathbf{v}\phi$ fluxes. Figure 9 shows that even at 36 h, there is already noticeable dispersion of energy downstream via these fluxes that offset the baroclinic processes organized by the maturing system. This cycle is similar to that found in the life cycle of a cyclone system in the Southern Hemisphere by Orlanski and Katzfey (1991) and discussed in a theoretical framework for downstream development by Orlanski and Chang (1992).

c. *Control simulation*

Although the simplified simulation is attractive in that it resembles closely an idealized case study, it is important to relate this findings to the more realistic case in which topography and diabatic surface and latent heat effects are all included. In a manner similar to the evolution shown in Fig. 6 for the simplified case, the eddy kinetic energy and fluxes for the control case at 12 and 36 h are shown in Fig. 11. At 12 h, the patterns are virtually identical to the simplified simulation. However, at 36 h, the K_e center over the region of interest is noticeably narrower due to reduced magnitude over the land area of western North America, and the

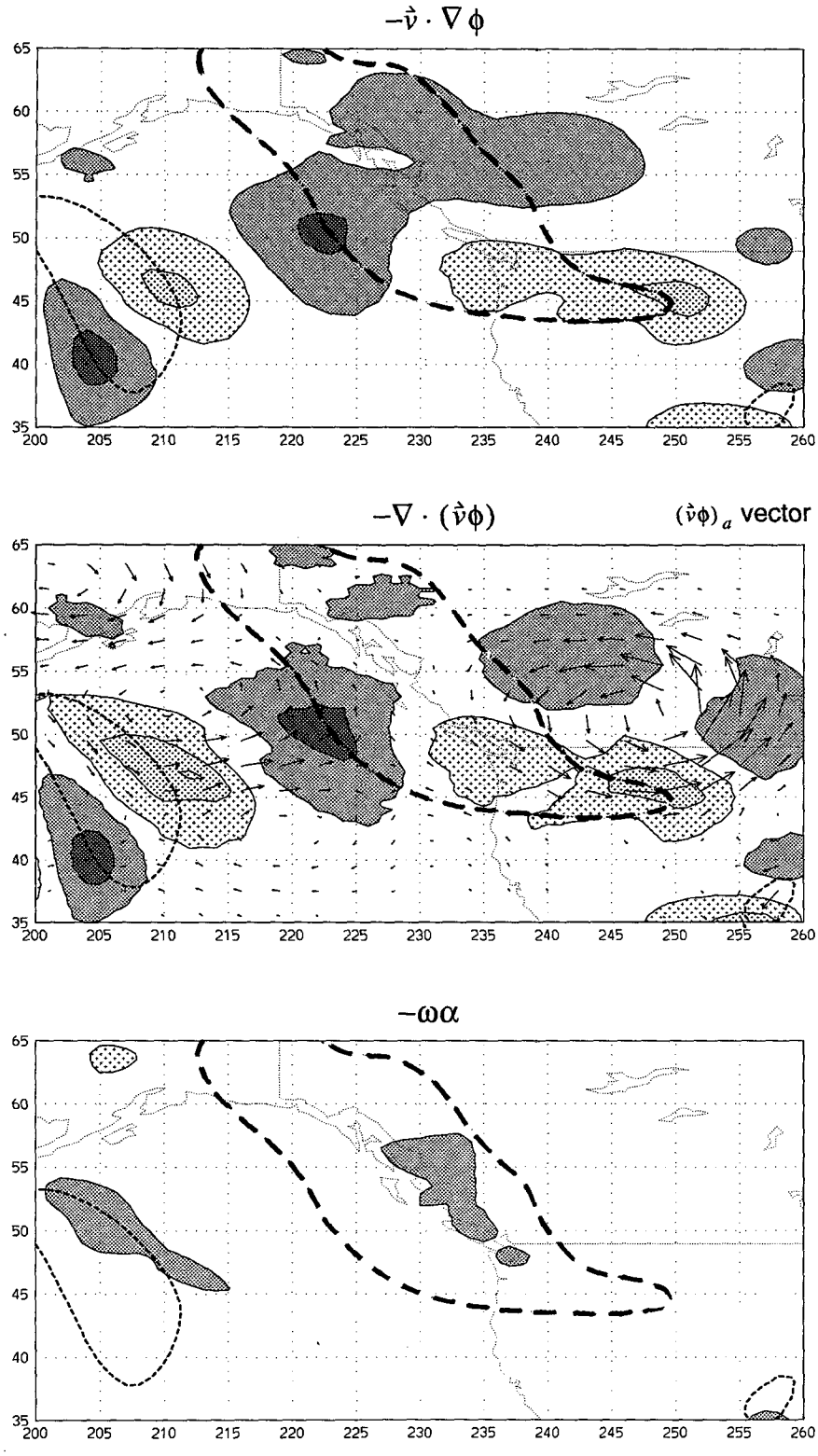

FIG. 9. Vertically averaged components of $-\mathbf{v}\cdot\nabla\phi$ for the simplified simulation at 1200 UTC 18 December (36 h). Units, stippling, and shading same as in Fig. 7.

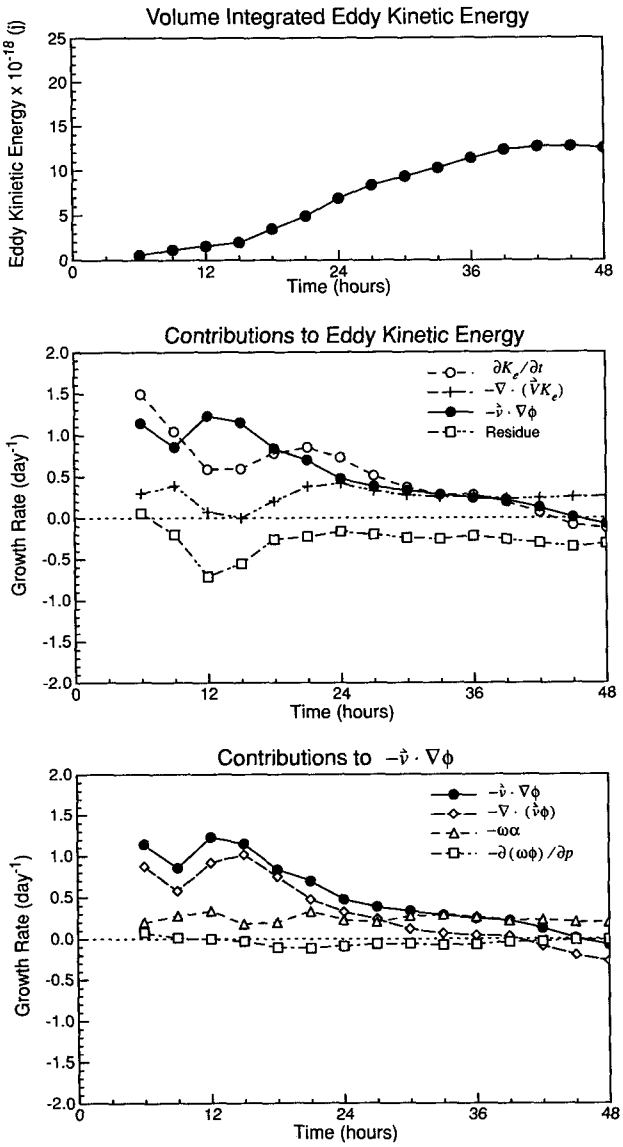

FIG. 10. Volume-integrated K_e and terms in the K_e equation for the simplified simulation over the period 0000 UTC 17 December to 0000 UTC 19 December (48 h). Top panel: volume-integrated eddy kinetic energy in units of 10^{18} J, integrated over the volume bounded by the heavy dashed curve in Figs. 6–9. Middle panel: contributions to eddy kinetic energy growth, expressed as a growth rate by dividing the volume integral of each quantity by the volume-integrated eddy kinetic energy. "Residue" is calculated by subtracting the energy flux divergence and eddy geopotential advection terms from the energy tendency term. Bottom panel: contributions to $-\mathbf{v}\cdot\nabla\phi$, also expressed as growth rates.

cyclonic circulation within the trough is substantially weaker. This is consistent with the differences in the 500-mb heights noted in Figs. 2 and 3, in which the control case displayed a weaker low but with sharper curvature in the area of Puget Sound. Note also that the energy centers in the central Pacific and over eastern Siberia are stronger in the control case, largely as a result of latent heat release. The fluxes from the Pacific energy center to the energy center of interest appear marginally stronger. It should be stressed that even in a case such as this, with strong diabatic and orographic processes taking place, the energy centers and energy fluxes as shown in Fig. 11 still provide valuable insight into the evolution of the system, giving an indication of where a new center may be generated and which of the existing centers will grow or decay.

The kinetic energy tendency and K_e flux divergence patterns for the control case at 12 h are virtually the same as that of the simplified case and are not shown. They reveal the same pattern of energy growth in the center via $-\mathbf{v}\cdot\nabla\phi$ and energy redistribution from the rear to the front of the center via $-\nabla\cdot(\mathbf{V}K_e)$. The decomposition of $-\mathbf{v}\cdot\nabla\phi$ at 12 h for the control case is shown in Fig. 12 and indicates that while $-\mathbf{v}\cdot\nabla\phi$ is substantially similar to that of the simplified case, the patterns of $-\nabla\cdot(\mathbf{v}\phi)$ and $-\omega\alpha$ are markedly more intense. In the case of $-\omega\alpha$, the intense areas in the western part of the region shown are related to strong latent heat release, while the weaker maximum along the Canadian coast is due to orographic uplift of warm air. The former of these maxima is also associated with a much larger divergence of the $(\mathbf{v}\phi)_a$ fluxes, which directly relates to the flux convergence near the entrance region of the K_e center of interest. This flux convergence is offset partially by weakly negative $-\omega\alpha$ induced by an indirect circulation, but the net effect on $-\mathbf{v}\cdot\nabla\phi$ is positive.

The decomposition of $-\mathbf{v}\cdot\nabla\phi$ at 36 h is shown in Fig. 13 and shows, once again, the greater intensity of the processes compared to the simplified case. At this time, however, both simulations display positive $-\omega\alpha$ over the Canadian coast, a consequence of sinking motion in the cold advection west of the trough that is common to both simulations and characteristic of west coast development, as opposed to East Coast development, in which rising motion in warm advection dominates $-\omega\alpha$. As at 12 h, the activity driven by latent heating over the western portion of the domain results in substantially greater $-\omega\alpha$ and correspondingly larger geopotential flux divergence compared to the simplified case. These fluxes are more strongly convergent on the western side of the energy center in the control case and, in fact, they seem to be more convergent over the volume as a whole. The stationary system to the west constitutes a major source of K_e for the K_e center via the $(\mathbf{v}\phi)_a$ fluxes, retarding the eastward progression of the center. The only other significant difference between the simulations is a reduced cyclonic pattern in the fluxes $(\mathbf{v}\phi)_a$ in the control case, probably associated with the deeper low in the simplified solution. There are some minor differences in the pattern of $-\omega\alpha$ that are mainly related to orographic lifting of cold air downstream of the center.

The evolution of the eddy kinetic energy budget for the control case is summarized in Fig. 14, calculated

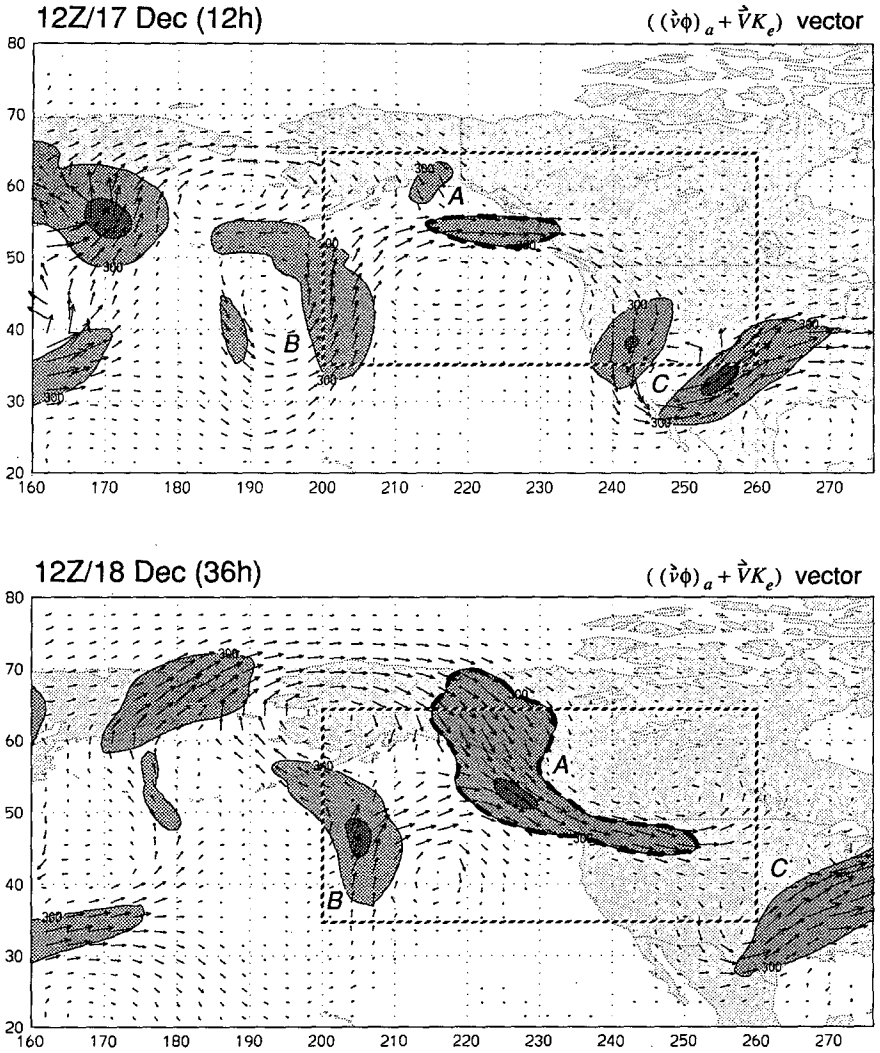

FIG. 11. Vertically averaged eddy kinetic energy and energy fluxes for the control simulation at 12 and 36 h. Shading same as Fig. 6. Dashed box indicates subregion to be shown in subsequent figures. The heavier dashed contour indicates the bounds of the specific volume of integration to be addressed later.

in the same manner as for the simplified case (see Fig. 10). As expected, the volume integral of K_e (upper panel) is noticeably reduced. Growth rates derived from the integrals of the terms in (4.2) are shown in the middle panel. For the first 30 h, the volume-integrated K_e tendency and $-\nabla\cdot(\mathbf{V}K_e)$ are both reduced in magnitude compared to the simplified case. The integrated $-\mathbf{v}\cdot\nabla\phi$ is larger in magnitude, and the residue has a larger magnitude (greater sink), as expected for a case with greater friction. The anomalously small values of residue around 24 h were found to be a product of a transient effect due to the barotropic conversion terms $[\mathbf{v}\cdot(\mathbf{v}\cdot\nabla\mathbf{v})_m$ and $\mathbf{v}\cdot(\mathbf{v}\cdot\nabla\mathbf{V}_m)]$, which, at these time scales, are difficult to interpret. (Other terms, such as the fluxes and $-\omega\alpha$, have analogs in the second-order terms of the energy cycle, and these problematic barotropic conversion terms disappear when averages are taken, and so there is no ready analog.) However, the evolution of energy budget still bears remarkable resemblance to that for the simplified case. Growth rates corresponding to the terms in (4.3) are shown in the bottom panel and indicate more substantial qualitative differences from the simplified case, despite the similarity of the $-\mathbf{v}\cdot\nabla\phi$ evolution. For the first 15 h, the lower levels of $-\nabla\cdot(\mathbf{v}\phi)$ in the control case are made up for by the larger values of $-\omega\alpha$, related to the orographic uplift of warm air. Beyond 15 h, the control case exhibits lower levels of $-\omega\alpha$ compared to the simplified case ($-\omega\alpha$ is effectively zero in the control case after 24 h), but greatly increased contributions from $-\nabla\cdot(\mathbf{v}\phi)$. As mentioned with regard to the $-\mathbf{v}\cdot\nabla\phi$ decomposition in Fig. 13, the source of the larger $(\mathbf{v}\phi)_a$

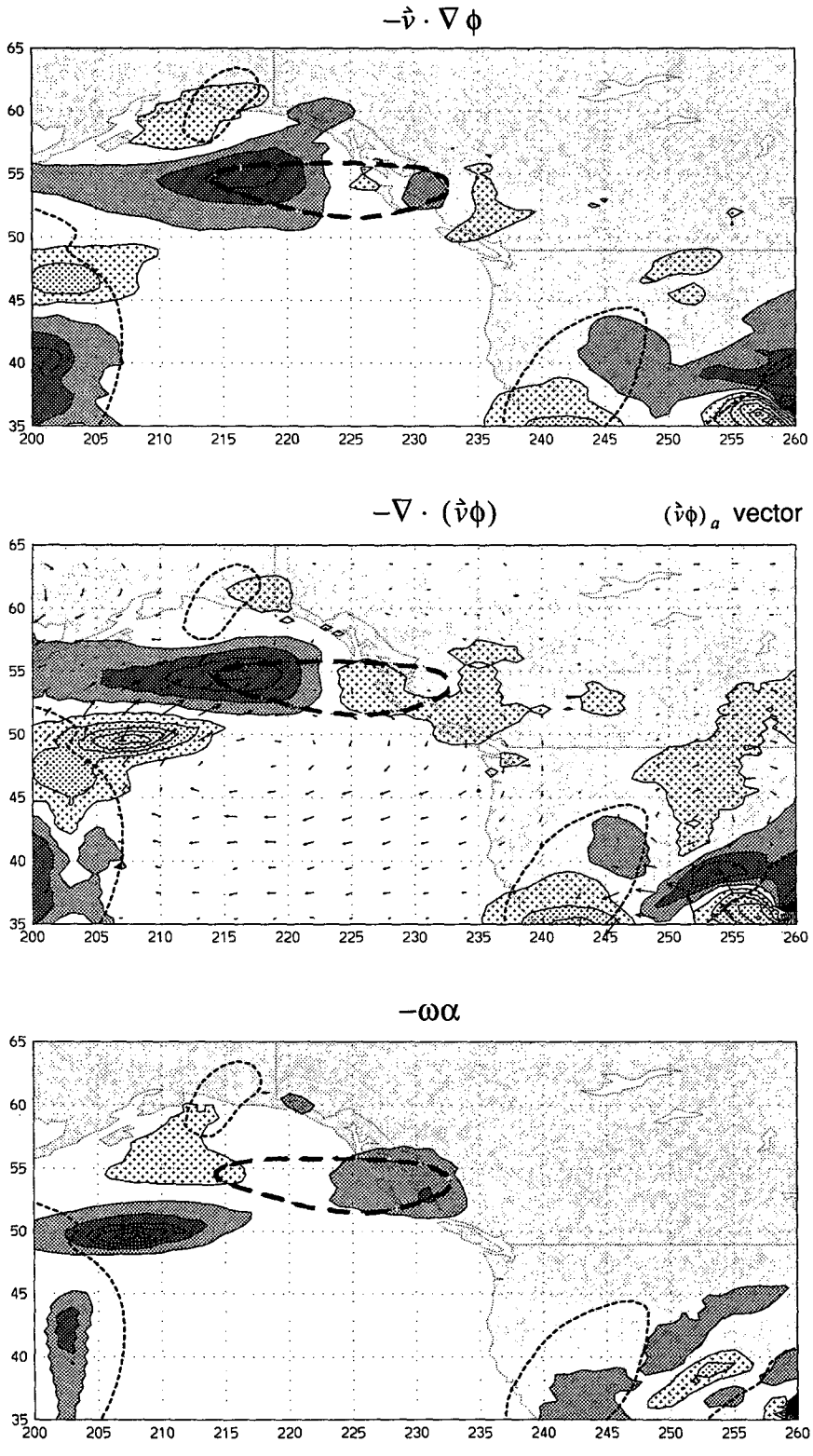

FIG. 12. Vertically averaged components of $-\mathbf{v} \cdot \nabla \phi$ for the control simulation at 1200 UTC 17 December (12 h). Units, stippling, and shading same as in Fig. 7.

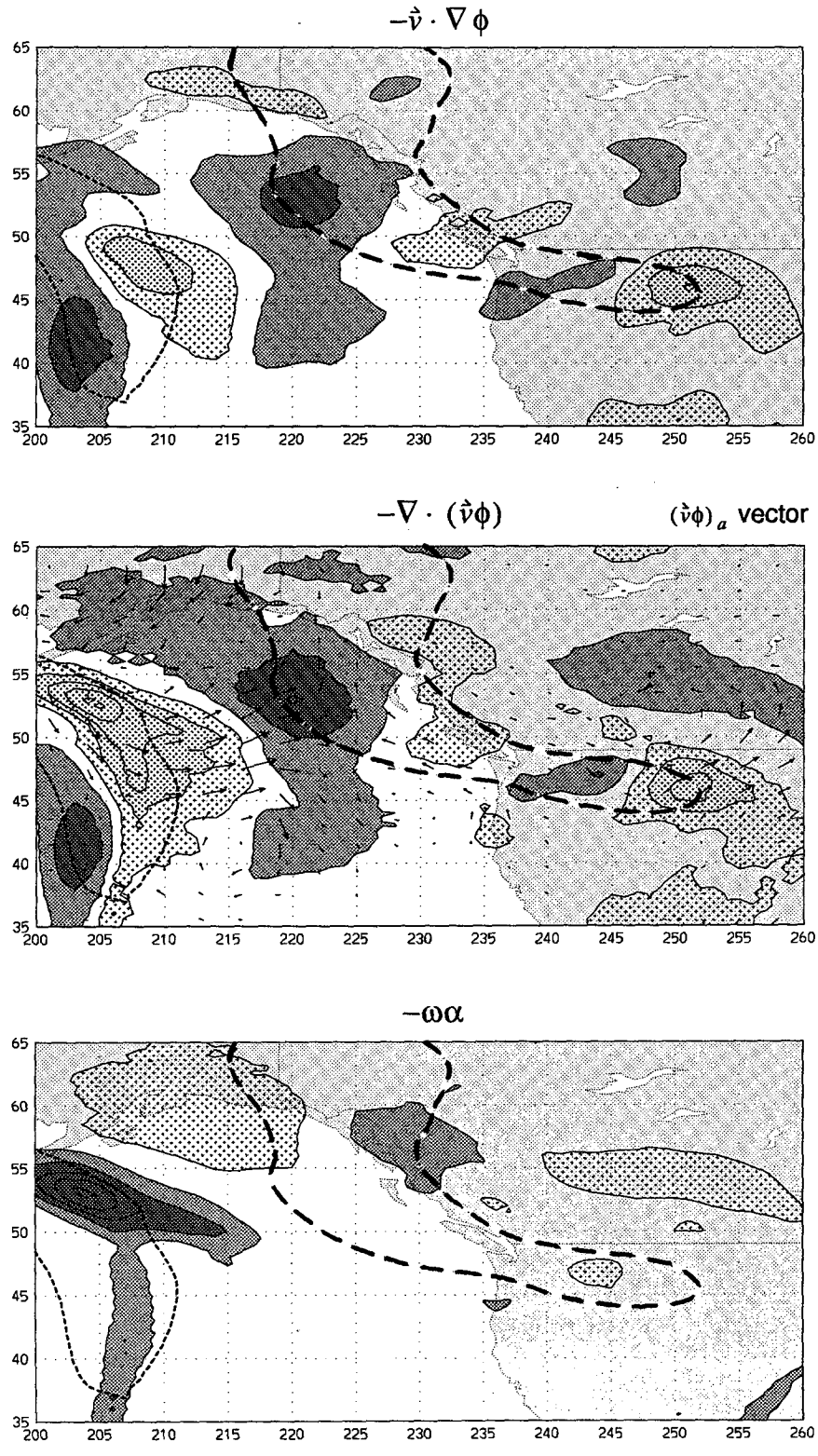

FIG. 13. Vertically averaged components of $-\mathbf{v} \cdot \nabla \phi$ for the control simulation at 1200 UTC 18 December (36 h). Units, stippling, and shading same as in Fig. 7.

fluxes in the control case is the strongly baroclinic activity associated with latent heating in the Pacific, west of the energy center under study, which is strongly radiating energy downstream. In both cases, however, the trend of $-\mathbf{v}\cdot\nabla\phi$ toward negative values at the end of the 48-h period is almost entirely a reflection of the tendency toward negative $-\nabla\cdot(\mathbf{v}\phi)$ once the storm has reached its maximum amplitude. In other words, the decay of the energy center is accomplished primarily by the dispersion of energy via $(\mathbf{v}\phi)$.

d. Vertical distribution of $-\nabla\cdot(\mathbf{v}\phi)$ and $-\omega\alpha$

The results of Orlanski and Chang (1993) showed that downstream development dominates the evolution of energetics at upper levels, while baroclinic conversion is more intense in the lower layers of the atmosphere. To better quantify the vertical distribution of baroclinic generation and geopotential flux divergence as discussed in connection with Figs. 11 and 13, vertical integrals of the same fields have been divided into two layers, 50–600 mb and 600 mb to the surface, and the results are shown in Figs. 15 and 16. The vertical integrals for each layer were normalized by the depth of the entire column from 50 mb to the surface, so that their sum of the two layers is identical to the averages presented in the previous sections. The results for both the simplified and control solutions in the 50–600-mb layer at 36 h are shown in Fig. 15. Clearly, flux divergence effects completely dominate $-\mathbf{v}\cdot\nabla\phi$ at upper levels in both cases, with significant $-\omega\alpha$ only in the baroclinically active region in the Pacific in the control case. Note that the fluxes are almost entirely in the downstream direction (eastward). Contrast this with the situation in the lower layer, shown in Fig. 16, where not only is the $-\nabla\cdot(\mathbf{v}\phi)$ pattern reversed but the flux itself is in the upstream direction (westward), characteristic of the fluxes in baroclinic wave, as discussed in Orlanski and Chang (1993). In virtually all instances, however, the magnitude of $-\nabla\cdot(\mathbf{v}\phi)$ at the lower levels is less than the corresponding value (of opposite sign) aloft. At lower levels, the magnitude of $-\omega\alpha$ is nominally comparable to $-\nabla\cdot(\mathbf{v}\phi)$, with the control case possessing a somewhat more vigorous pattern, due mainly to latent heating. Thus, this analysis shows that downstream energy dispersion via $(\mathbf{v}\phi)$ fluxes dominated baroclinic processes aloft for both simulations, while at low levels the processes were more comparable, and with the flux divergence being of opposite sign to that aloft. The flux convergence in the lower levels of the control case was a maximum where baroclinic conversion was also a maximum. It should be pointed out that for storms in which the lower-layer upstream fluxes become important, *upstream* development can also follow (Thorncroft 1989).

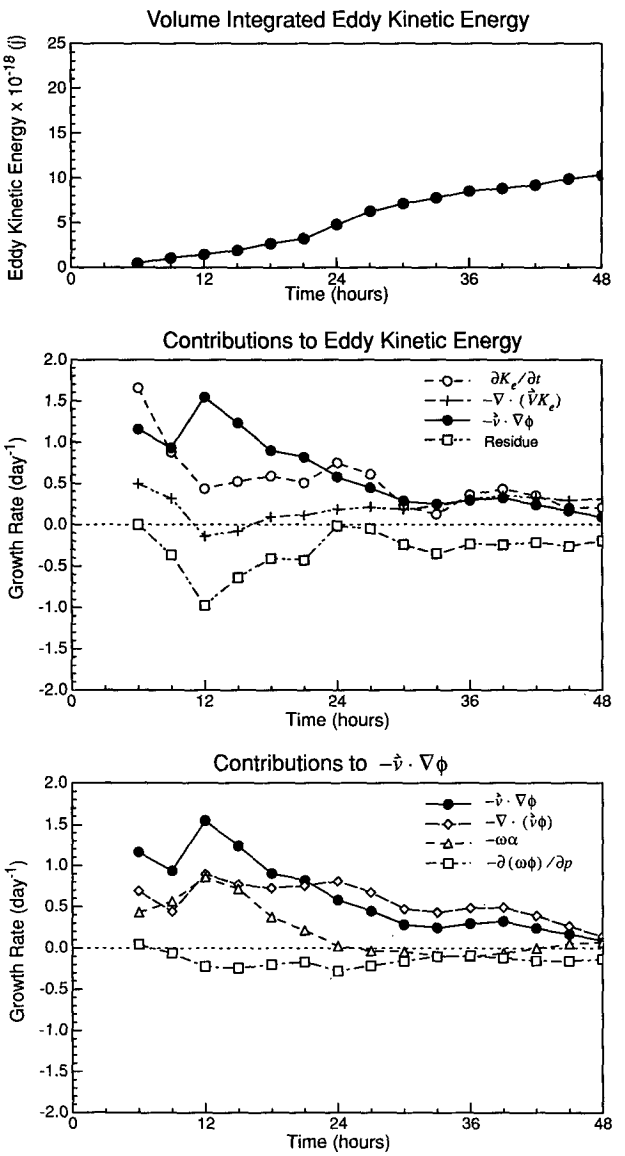

FIG. 14. Volume-integrated K_e and terms in the K_e equation for the control simulation over the period 0000 UTC 17 December–0000 UTC 19 December (48 h). Quantities and units same as in Fig. 10.

5. Summary

Recent studies have demonstrated the importance of downstream development, expressed in terms of ageostrophic geopotential fluxes, not only in the life cycle of transient eddies but also in the maintenance of storm tracks (Chang and Orlanski 1993), where flux convergence constitutes a primary energy source for the growth of eddies far downstream from the principal baroclinic energy source. These fluxes are also the primary means by which these eddies decay, transferring their energy to the next system downstream, mainly at upper levels. As new eddies mature, they induce low-level circulations, tapping whatever baroclinicity exists locally, with their subsequent growth dependent on the amount of baroclinic energy available. This general process, in which unstable baroclinic eddies disperse

energy downstream, has been named "downstream baroclinic development," (DBD) in contrast to downstream development associated with energy dispersion by barotropic neutral Rossby waves. A regression analysis in a recent study (Chang 1993) has confirmed the importance of downstream baroclinic development in maintaining the eastern part of the Pacific storm track.

To further corroborate this hypothesis, a case study was performed in which the development of a deep trough–ridge system at the eastern end of the Pacific storm track was simulated and analyzed in great detail. The GFDL LAHM model was used to simulate the initiation of this strong system that led to a record cold outbreak over the western United States in late December 1990. A control simulation demonstrated considerable skill in capturing the important features of this event. A "simplified" simulation was conducted in which all land surface, surface heat fluxes, and latent heating effects were removed, and a spatially uniform surface drag coefficient was used. The result was a somewhat stronger storm, indicating that orographic influences, land–sea contrast, surface heating effects, and latent heating, as a whole, actually inhibited storm development to some extent. However, the basic ridge–trough development was reproduced, and the removal of these influences greatly simplified the analysis of the energetics of the developing storm, as well as provided a base solution for the quantification of the contributions from diabatic effects and surface boundary forcing in the control simulation.

An energy budget equation was derived and applied, and energy generation via $-\mathbf{v}\cdot\nabla\phi$ was broken down into a baroclinic term, $-\omega\alpha$, and a "dispersion" term, $-\nabla\cdot(\mathbf{v}\phi)$. While baroclinic processes did contribute to the growth of eddy kinetic energy in both simulations, early growth of the K_e center over western North America was dominated by the convergence of the geopotential fluxes, $-\nabla\cdot(\mathbf{v}\phi)$. Baroclinic conversion, mainly due to descending cold air, became the primary source of energy only after the development was well under way, a sequence of events typical of downstream baroclinic development. The decay of the storm in both simulations was the result of flux divergence after the storm reached maturity, although this decay was somewhat delayed in the control simulation because kinetic energy generated by latent heat release in an upstream eddy produced larger fluxes into the system.

Results from this and previous studies (Orlanski and Katzfey 1991; Orlanski and Chang 1993; Chang and Orlanski 1993) suggest that local energy budgets such as that presented in this paper could be an important diagnostic tool for both the basic understanding of baroclinic systems and for analyzing discrepancies between forecasts and verification. The ability to identify storm systems that are as much a product of downstream baroclinic development as they are of purely local conditions

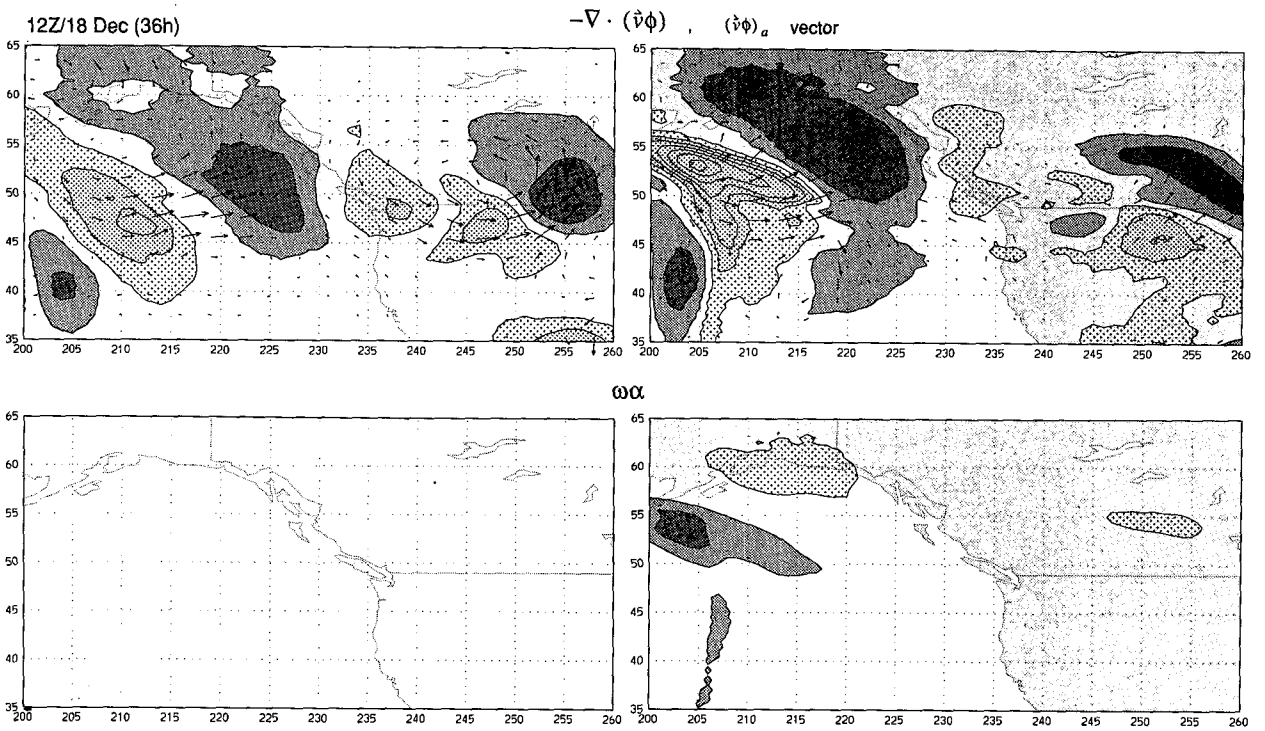

FIG. 15. Vertically integrated eddy geopotential flux convergence (top panels) and baroclinic conversion (bottom panels) at 1200 UTC 18 December (12 h). Integral is from 50 to 600 mb and is normalized by the entire depth of the atmosphere (50 mb to surface). Left panels are the simplified simulation; right panels are the control simulation. Vectors, stippling, and shading same as in Fig. 8.

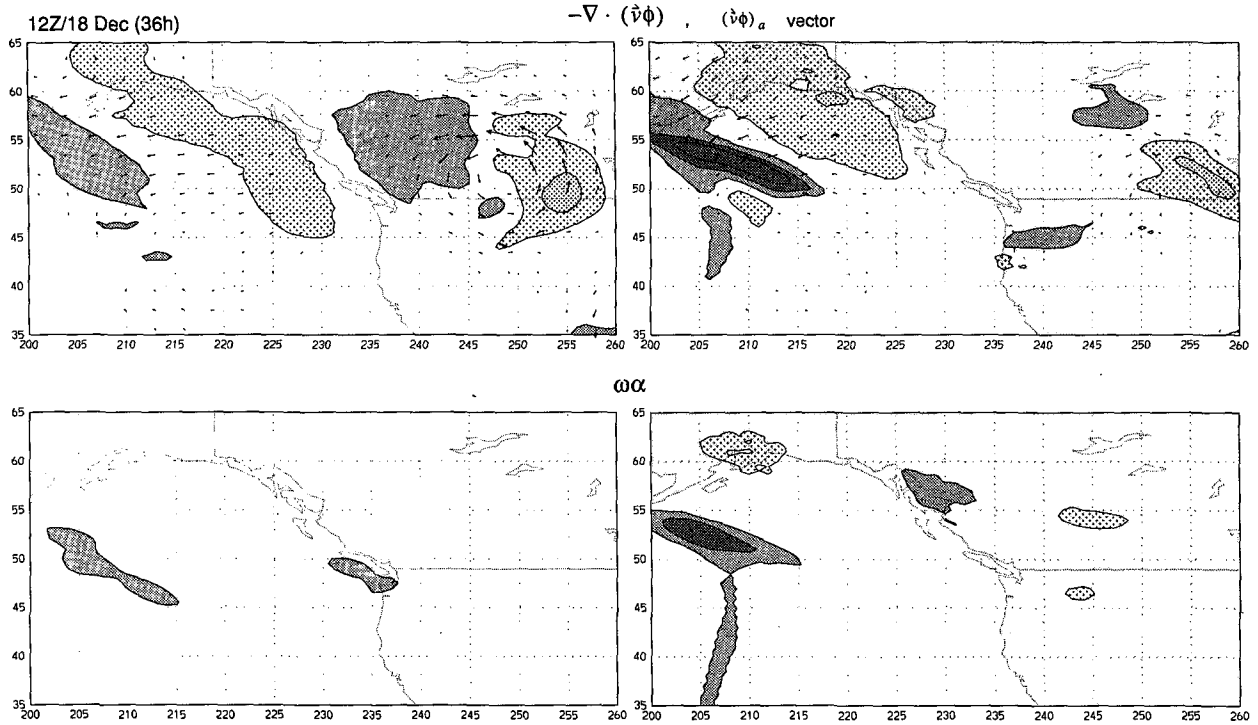

should have a considerable impact on our prediction capabilities. Recently, Lee and Held (1993) demonstrated, through GCM simulations and analyses of the Southern Hemisphere storm track, that baroclinic eddies could evolve in packets that can propagate considerable distances around the globe. While each of these baroclinic eddies grows and decays inside the packet over a period of a few days, the packet itself can have a life span of a several weeks, maintained mainly through downstream baroclinic development. Despite the fact that the special conditions by which these packets form are not yet completely understood, their stability implies that they have considerable predictability. Knowledge of which areas around the globe are more prone to downstream baroclinic development could result in a considerable improvement in forecast skill for cyclone systems in those regions, since upstream eddies can be detected days in advance. Toward this end, it would probably be most useful to define regions around the globe where downstream baroclinic developments are most important. An index of this sort is under investigation.

In a more applied sense, errors produced by operational numerical models could be tied, in some cases, to the inability of the model to produce the correct fluxes. Analysis of the ageostrophic geopotential fluxes, in conjunction with the distribution of baroclinic conversion, could help to determine the sources of error in forecast storm intensity and speed. Model forecast error may be due to faulty initial conditions that misrepresent the vertical structure of the wave. Since the downstream fluxes depend significantly on the vertical structure of the wave (deep or shallow), faulty initial conditions might also misrepresent those fluxes and thereby affect the subsequent evolution of the system. Our ability to improve any given forecast is likely to depend on whether the system is purely baroclinic or a product of downstream baroclinic development. Initialization schemes that provide accurate energy fluxes could translate directly into improved skill in predicting downstream baroclinic development cases.

Downstream baroclinic development could also play an important role in regions of strong surface baroclinicity, such as the coastal areas of the eastern United States, where intense cyclogenesis occurs that is characteristic of so-called class-B cyclogenesis (Petterssen and Smebye 1971). The relationship between downstream development and class-B cyclogenesis is the subject of continuing research, as well.

Acknowledgments. The authors wish to express their thanks to Brian Gross and Hisashi Nakamura for their input to the initial drafts of this work, as well as to the anonymous reviewers whose comments contributed to its readability and clarity in explaining some rather new concepts. We also would like to thank Fred Sanders for both his candid comments and his very prompt attention during the review process.

REFERENCES

Blackmon, M. L., Y. H. Lee, and J. M. Wallace, 1984a: Horizontal structure of 500 mb height fluctuations with long, intermediate, and short time scales. *J. Atmos. Sci.*, **41**, 961–979.

——, ——, ——, and H. H. Hsu, 1984b: Time variation of 500 mb height fluctuations with long, intermediate, and short time scales as deduced from lag-correlation statistics. *J. Atmos. Sci.*, **41,** 981–991.

Boyle, J. S., and T.-J. Chen, 1987: *Synoptic Aspects of the Wintertime East Asian Monsoon; Section II5: Monsoon Meteorology,* Oxford University Press, 544 pp.

Chang, K. M., 1993: Downstream development of baroclinic waves as inferred from regression analysis. *J. Atmos. Sci.*, **50,** 2038–2053.

——, and I. Orlanski, 1993: On the dynamics of storm tracks. *J. Atmos. Sci.*, **50,** 999–1015.

Cressman, G. P., 1948: On the forecasting of long waves in the upper westerlies. *J. Meteor.*, **5,** 44–57.

Hovmöller, E., 1949: The trough and ridge diagram. *Tellus,* **1,** 62–66.

Hsu, H.-H., and J. M. Wallace, 1985: Vertical structure of wintertime teleconnection patterns. *J. Atmos. Sci.*, **42,** 1693–1710.

Joung, C. H., and M. H. Hitchman, 1982: On the role of successive downstream development in east Asian polar air outbreaks. *Mon. Wea. Rev.*, **110,** 1224–1237.

Lee, S., and I. M. Held, 1993: Baroclinic wave packets in models and observations. *J. Atmos. Sci.*, **50,** 1413–1428.

Lim, G. H., and J. M. Wallace, 1991: Structure and evolution of baroclinic waves as inferred from regression analysis. *J. Atmos. Sci.*, **48,** 1718–1732.

Longuet-Higgins, M. S., 1964: On group velocity and energy flux in planetary wave motions. *Deep-Sea Res.*, **11,** 35–42.

Mesinger, F., 1977: Forward–backward scheme and its use in a limited area model. *Contrib. Atmos. Phys.*, **50,** 200–210.

——, 1981: Horizontal advection schemes of a staggered grid—An enstrophy and energy conserving model. *Mon. Wea. Rev.*, **109,** 467–478.

Miyakoda, K., and J. Sirutis, 1977: Comparative integrations of global models with various parameterizations: Processes of subgrid vertical transport. *Contrib. Atmos. Physics,* **50,** 445–487.

Namias, J., and P. F. Clapp, 1944: Studies of the motion and development of long waves in the westerlies. *J. Meteor.*, **1,** 57–77.

Orlanski, I., and K. M. Chang, 1993: Ageostrophic geopotential fluxes in downstream and upstream development of baroclinic waves. *J. Atmos. Sci.*, **50,** 212–225.

——, and B. D. Gross, 1993: Orographic modification of cyclone development. *J. Atmos. Sci.*, in press.

——, and J. J. Katzfey, 1987: Sensitivity of model simulations for a coastal cyclone. *Mon. Wea. Rev.*, **115,** 2792–2821.

——, and ——, 1991: The life cycle of a cyclone wave in the Southern Hemisphere. Part I: Eddy energy budget. *J. Atmos. Sci.*, **48,** 1972–1998.

Pedlosky, J., 1987: *Geophysical Fluid Dynamics.* Springer-Verlag, 710 pp.

Petterssen, S., and S. J. Smebye, 1971: On the development of extratropical cyclones. *Quart. J. Roy. Meteor. Soc.*, **97,** 457–482.

Simmons, A. J., and B. J. Hoskins, 1979: The downstream and upstream development of unstable baroclinic waves. *J. Atmos. Sci.*, **36,** 1239–1260.

——, J. M. Wallace, and G. W. Branstator, 1983: Barotropic wave propagation and instability, and atmospheric teleconnection patterns. *J. Atmos. Sci.*, **40,** 1363–1392.

Smith, B. R., and S. L. Mullen, 1993: An evaluation of sea level cyclone forecasts produced by NMC's nested-grid model and global spectral model. *Wea. Forecasting,* **8,** 37–56.

Thorncroft, C. D., and B. J. Hoskins, 1990: Frontal cyclogenesis. *J. Atmos. Sci.*, **47,** 2317–2236.

Uccellini, L. W., D. Keyser, K. F. Brill, and C. H. Wash, 1985: The President's Day cyclone of 18–19 February 1979: Influence of upstream trough amplification and associated tropopause folding on rapid cyclogenesis. *Mon. Wea. Rev.*, **113,** 962–987.